Beyond conventional characterization

Defect engineering role for sensitivity and selectivity of room-temperature UV-assisted graphene-based NO_2 sensors

Peña, Álvaro; López-Sánchez, Jesús; Sacco, Leandro; Vollebregt, Sten; Marqués-Marchán, Jorge; Horrillo, M. Carmen; Marín, Pilar; Matatagui, Daniel

DOI
10.1016/j.talanta.2024.127507

Publication date
2025

Document Version
Final published version

Published in
Talanta

Talanta 286 (2025) 127507

Contents lists available at ScienceDirect

Talanta

journal homepage: www.elsevier.com/locate/talanta

Beyond conventional characterization: Defect engineering role for sensitivity and selectivity of room-temperature UV-assisted graphene-based NO_2 sensors

Álvaro Peña [a,*], Jesús López-Sánchez [b], Leandro Sacco [c], Sten Vollebregt [c], Jorge Marqués-Marchán [d], M. Carmen Horrillo [e], Pilar Marín [a,f], Daniel Matatagui [a,f,**]

[a] Instituto de Magnetismo Aplicado, UCM-ADIF, Las Rozas, 28230, Spain
[b] Department of Electroceramics, Instituto de Cerámica y Vidrio (ICV), CSIC, 28049, Madrid, Spain
[c] Department of Microelectronics, Delft University of Technology, Feldmannweg 17, 2628, CT Delft, the Netherlands
[d] Instituto de Ciencia de Materiales de Madrid (ICMM), CSIC, 28049, Madrid, Spain
[e] SENSAVAN, Instituto de Tecnologías Físicas y de la Información (ITEFI), CSIC, 28006, Madrid, Spain
[f] Departamento de Física de Materiales, Universidad Complutense de Madrid (UCM), 28040, Madrid, Spain

ARTICLE INFO

Handling editor: Agata Michalska

Keywords:
Graphene-based materials
Gas sensors
Defect engineering
Ultraviolet
Nitrogen dioxide
Carbon monoxide

ABSTRACT

The term graphene-based gas sensors may be too broad, as there are many physicochemical differences within the graphene-based materials (GBM) used for chemiresistive gas sensors. These differences condition the sensitivity, selectivity, recovery, and ultimately the sensing performance of these devices towards air pollutants. Continuous ultraviolet irradiation aids in the desorption of gas molecules and enhances sensor performance. Under these conditions, the devices from this work can reliably monitor NO_2 and CO at room temperature, below the human-recommended exposure limits, presenting NO_2 LoD down to ~20 ppb. By selecting GBMs with different levels of defectivity, which influence gas adsorption dynamics, and through comprehensive characterization, including D, D′, D″, 2D, and G Raman bands, graphene-based gas sensors can be tailored to meet specific sensing requirements. This study examines five different non-oxidized GBM to develop tools and gain a deeper understanding of the relationships between GBM properties and their sensing performance. This research introduces a new standard for defect assessment, moving beyond graphene's D and G Raman band intensity ratio, to facilitate the successful integration of graphene-based gas sensors into everyday applications, such as environmental monitoring and industrial safety, and potentially impacting other 2D materials, thereby reducing health risks associated with air pollution.

1. Introduction

Nitrogen dioxide (NO_2) and carbon monoxide (CO) pose a significant problem due to its widespread presence as a byproduct of combustion processes in vehicles, power plants, and industries [1]. NO_2 concentrations in urban areas may reach levels up to around 0.1–1 parts per million (ppm) [2], while studies have shown that even relatively low exposures, such as 0.1 ppm for 24 h or annual mean exposures below that – time-dependent but sub-ppm daily – are associated with increased hospital admissions and higher mortality rates [3,4]. Vulnerable populations, including children, adolescents, the elderly, and those with respiratory conditions, are particularly susceptible to these health risks [5]. CO, on the other hand, interferes with the blood's ability to carry oxygen leading to symptoms like headaches and dizziness that can ultimately be fatal, with approximately 400 yearly deaths in the USA alone [6]. Recommended maximum exposure levels are limited to 3.4 ppm for 24 h or 30 ppm for 1 h [7].

The World Health Organization (WHO) recently revealed that almost all of the global population (<90 %) breathe air that exceeds their guideline limits and contains high levels of pollutants, with low- and middle-income countries suffering from the highest exposures.[1] Henceforth, highly sensitive and cost-effective gas detection devices are

* Corresponding author.
** Corresponding author. Instituto de Magnetismo Aplicado, UCM-ADIF, Las Rozas, 28230, Spain.
E-mail addresses: alvapena@ucm.es (Á. Peña), daniel.m.c@ucm.es (D. Matatagui).

[1] World Health Organization, Air pollution, Https://Www.Who.Int/Health-Topics/Air-Pollution#tab=tab_1 (2020).

https://doi.org/10.1016/j.talanta.2024.127507
Received 12 October 2024; Received in revised form 23 December 2024; Accepted 30 December 2024
Available online 1 January 2025

essential to address the problems associated with air pollutants. These devices can accurately measure and track NO_2 or CO concentrations in the atmosphere, aiding in the timely identification of pollution sources and monitoring concentration changes over time [8]. By enabling early detection and intervention, they play a crucial role in implementing effective strategies to mitigate the adverse effects of air pollution on both human health and the environment.

Graphene and other graphene-based materials (GBM) are a recent alternative among the active materials for chemiresistive gas sensors [9]. Its large specific surface (2630 m^2/g), high conductivity, and low noise-to-signal ratio make graphene and GBM ideal candidates for gas sensing applications [10]. Over a decade has passed since the first report of a graphene-based gas sensor, with a sensitivity down to a single molecule under highly controlled conditions [11]. During the following years, the number of similar devices reported for detecting different gaseous molecular species under conditions closer to real-life applications has increased dramatically. These graphene-based devices have demonstrated their potential for room temperature sensing NO_2, CO, sulfur dioxide (SO_2) or ammonia (NH_3), among other analytes, and significantly, the research interest in the material has increased [12,13].

However, graphene-based sensors are not without drawbacks. One well-known issue is partial recovery, as the analyte molecules attached to the surface of the sensor do not easily desorb or do so within a short time. Consequently, the performance of the device tends to degrade after each new analyte exposure [14]. The purpose of UV irradiation is to clean and restore the device [15–17] simulating the effect of temperature-forced recovery after the analyte adsorption [11]. Interestingly, continuous UV irradiation has been recently proposed as a method to not only promote faster and more complete desorption but also to enhance the sensing performance of the device at room temperature [18,19].

On the other hand, various approaches have been explored to enhance the sensitivity and selectivity of graphene-based devices. Sensitivity refers to the change in the resistivity of the sensor in the presence of the analyte, while selectivity is the ability to produce differentiated responses to similar analytes [20–22]. One such approach involves doping and functionalization, which entails introducing compounds or elements, such as metallic nanoparticles, with high reactivity towards the analytes [23,24]. Another promising approach is defect engineering, which aims to improve sensing performance by modifying the structure of graphene itself through the introduction and/or generation of structural defects [25,26].

In this scenario, two central issues have emerged. Firstly, the prevalent method of quantifying defects using only the I(D)/I(G) Raman ratios often neglects the specific nature of these defects (see Table S1 in the Supporting Information). This approach may inadvertently overlook the diversity and characteristics of defects that can exist within GBM, as different defects and bonding sites exhibit different bonding energies to the incoming analytes [27]. In addition, the I(D)/I(G) ratio can be also affected by elemental functionalization, not just by defect engineering [28]. Therefore, the nature of defects can be masked by a simple I(D)/I(G) ratio and it is important to understand the origin of its change and how can impact sensing performance [23]. Secondly, many gas sensor studies utilize GBM that – being these not strictly pristine graphene – possess unique physicochemical properties [29]. However, the practice of categorizing such materials under the broad label of 'graphene' may fail to adequately account for the nuanced relationship between their inherent nature and sensing capabilities.

Therefore, based on the hypothesis that defect engineering demands a more careful characterization and understanding of the correlation between the GBM properties and their sensing performance, this study compares different non-oxidized GBM used in gas sensor development.

- Mechanically exfoliated graphene – great structural quality and close to pristine graphene [30].
- Chemical vapor deposition (CVD)-grown multilayer graphene (MLG) – A relatively ordered stacking of graphene layers grown on top of each other where the structural quality may depend on the growth temperature [31].
- Ball-milled few-layered mesoporous graphene (FLMG) – Agglomerates of relatively defective few-layered graphene [32].

To provide a comprehensive understanding of how different types of defects influence the sensing performance of graphene-based gas sensors, it is essential to characterize these defects. By correlating defects with sensor performance through rigorous experimental studies and data analysis, we can gain valuable insights into the physicochemical characteristics of graphene-based materials. This knowledge will drive the design of materials with tailored properties, optimizing sensor sensitivity and selectivity for specific analytes and paving the way for the development of advanced next-generation sensor materials.

2. Materials and methods

2.1. Material's fabrication

Pristine graphene was produced by micromechanical exfoliation of natural graphite blocks as described elsewhere [25], following the method first described in 2004 [30].

MLG was synthesized by CVD on a pre-patterned Mo catalyst in an AIXTRON BlackMagic Pro reactor. 20 sccm of methane (CH_4) was used as a carbon feedstock for 20 min in Ar/H_2 atmosphere at 25 mbar, and three different values of growth temperature were employed, i.e., 850, 890, and 935 °C [33,34].

FLMG was obtained using a high-energy ball-milling technique. Briefly, 1 g of graphite (Natural, −325 Mesh, 99.8 % Metal Basis from Alfa Aesar) was milled in an oscillatory mill (MM400, Retsch GmbH) with a powder-to-ball ratio of 1:25 at 1500 rpm for 100 min. The process is fully described elsewhere [35]. The milled product was then suspended in 1-Methyl-2-Pyrrolidone (Sigma-Aldrich, 99.0 %) to a concentration of 1 mg/ml by sonicating for 1 h. The suspension was centrifugated for 15 min at 9000 rpm and the supernatant was collected.

2.2. Characterization techniques

The obtained material was investigated by confocal Raman spectroscopy using a Witec ALPHA model 300RA (Oxford Instruments) with a Nd:YAG green laser source of 532 nm in p-polarization. The optical resolution is ~200 nm in lateral and ~500 nm in vertical dimensions. Intensity Raman mappings of representative regions were carried out for selected samples with a 100x objective lens (numerical aperture of 0.95). Raman spectra were acquired every 500 nm with an integration time of 1.5 s, using a 600 gr/mm grating with a spectral resolution of ~0.02 cm^{-1}. The output laser power employed was 0.2 mW to avoid sample damage or overheating effects [36], previously calibrated with a Thorlabs potentiostat. Raman data were examined and analyzed by the Witec Plus Software (version 2.08). The spectra presented here are the mean values of an integrated area to prevent the effects of local inhomogeneities. The surface morphology of the samples after growth was measured by atomic force microscopy (AFM) employing an ND-MDT AURA setup, operating in semi-contact mode with a poly-Si HA-NC cantilever having a radius <10 nm, at a rate of 0.60 Hz and acquiring 256 lines on scanned areas of 25 μm^2 [37].

Scanning electron microscopy (SEM; JEOL 7600F), was used to characterize the morphological and structural properties of both the materials and the devices.

2.3. Sensing device preparation

The mechanically exfoliated graphene flakes were transferred to a silicon wafer covered by 90 nm thick thermally grown SiO_2 [25]. The

device is denoted as ME in reference to the production method.

The CVD-based devices were fabricated by adopting the transfer-free process, further detailed elsewhere [38]. Through a few lithographic steps, a sputtered and patterned Mo layer (50 nm) was wet-etched after the growth of MLG. That way, MLG dropped on the SiO2/Si substrate at the pre-defined positions. Next, the graphene deposits were contacted using 10/100 nm Cr/Au deposited using e-beam evaporation and patterned using a lift-off process (Fig. S1 in the Supporting Information). The devices are named CVD850, CVD890 and CVD935 according to the temperature at which the material was grown.

FLMG was dispersed in n-methyl-2-pyrrolidone (NMP; Sigma Aldrich) at a concentration of 1 mg/mL in a sonication bath until a stable suspension was obtained. The FLMG-based was fabricated using dielectrophoresis-assisted (10 kHz, 10 Vpp) drop-casting deposition onto an interdigitated electrodes (IDE) substrate (DRP-G-IDEAU10, DropSens). The device is referred to as BM100, according to synthesis method characteristics, ball-milled for 100 min.

2.4. Gas setup

The sensing devices were placed in a 3D-printed PLA airtight cell (with a volume of ~10 mL) connected to an automated gas generator. The airflow inside the cell was set to 100 mL/min, and the measurements were performed by exposing the sensor to a mixture of the target gas NO_2 and CO (from 1 ppm to 10 ppm balance air cylinders, respectively) and synthetic dry air as a carrier, which was also used for purging. All gases were provided by Nippon Gases, Spain. Mass flow controllers adjusted the concentration of each gas sample through custom-made LabView software that simultaneously monitors the device's resistance using a digital multimeter (Keithley 2001). A 275 nm ultraviolet light-emitting diode (SeoulViosys CA3535 - CUD7GF1B) was placed inside the chamber to irradiate a power density of 34 W/m^2. Similar wavelength and power density conditions have been reported in previous graphene-based gas sensor examples [39,40]. A schematic representation of the experimental setup is represented in Fig. 1.

2.5. Gas sensing characterization

Firstly, the I–V curves corresponding to the ME [25], CVD (850, 890 and 935) [41], and BM100 (Fig. S2 in the Supporting Information) devices exhibit consistent characteristics with resistors, offering linear behaviors that ensure accurate and reliable readings. After the devices were subjected to photoactivation and reached a stable state, the sensors exhibited the following resistances: ME showed a resistance of 3.3 kΩ, CVD850 measured 2.7 MΩ, CVD980 registered 33 kΩ, CVD935 had a resistance of 98 kΩ, and BM100 displayed 120 Ω. These resistance values remained stable and consistent until the target gases were introduced into the system, indicating a reliable baseline prior to exposure to the gases of interest.

The device's response (Response(%)) refers to the immediate, time-dependent change in the sensor's electrical resistance when exposed to the gas [42]. It is reported as a relative percentage and described as the change of resistance (R) normalized to base resistance (R_0) in absolute value:

$$Response\ (\%) = \left| \frac{\Delta R}{R_0} * 100 \right| \quad (1)$$

In this context, "maximum response" refers to the maximum variation in response observed during the exposure phase. This definition inherently depends on the exposure time unless the response reaches saturation. However, it is employed here as a quantitative measure for comparing sensor performances.

Before every test, the devices were stabilized with running dry air until no significant variations of their resistance were appreciable, i.e., when the device had reached an equilibrium with the carrier gas. These conditions are regarded as either initial or baseline conditions. R_0 is thus defined as the measured resistance immediately before the first analyte exposure.

Evaluation of the device's sensing performance was done through two different sequences. First, three consecutive exposures to the same concentration of the analyte to obtain an arithmetic mean response with its standard deviation. This sequence included a baseline followed by three cycles of 25-min exposure to the analyte and a 15-min recovery phase, in which only the carrier gas passed through the device. Second, a

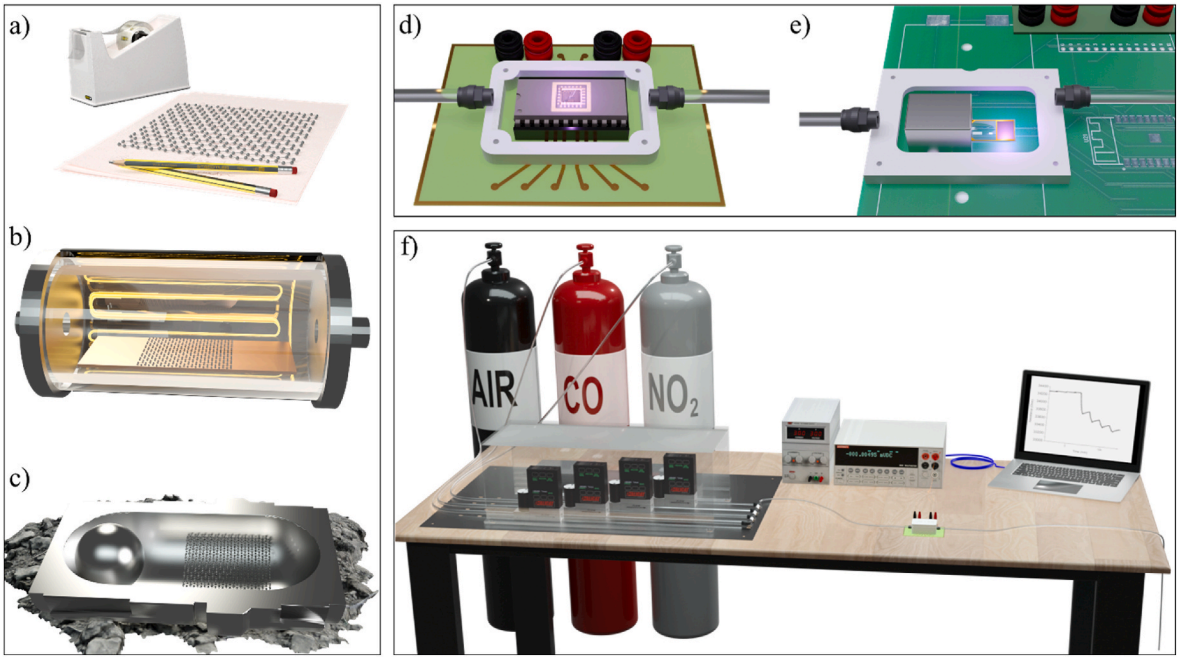

Fig. 1. Representation of the experimental work. Including a) mechanical exfoliation, b) CVD and c) ball-milling synthesis methods, d) sensing platform for ME and CVD devices, e) IDE platform for BM100 device and f) illustration of the testing line.

calibration curve consisting of cycles with the same phase duration as the previous exposure and recovery ones, with different analyte concentrations. This sequence was only performed for NO_2 to concentrations of 0.1, 0.15, 0.25, 0.40, 0.65 and 1 ppm. All sensing measurements were taken under constant UV irradiation.

The limit of detection (LoD) represents the lowest concentration of gas that can be reliably detected by the sensor. It is typically calculated according to Equation (2) [43,44]:

$$LoD_{(RMSnoise,Sensitivity)} = \frac{3*RMS\ noise}{Sensitivity} \quad (2)$$

Where the sensitivity (%/ppm), is extracted from the calibration curve and the RMS noise is the root mean squared noise of the device signal during blank measurement. The RMS noise is multiplied by three in Equation (2) to ensure the reliability of the LoD [45,46].

2.6. Data correlation

In addition to the experimental characterization, the results were mathematically treated to find relevant correlations, between the material physicochemical properties and the sensing performance of each device using the LASSO (Least Absolute Shrinkage and Selection Operator) method [47,48]. LASSO automatically identifies key features of the material relevant to the different target variables by setting up a linear regression model where each feature from characterization is assigned a coefficient. The non-zero coefficients correspond to the most effective variables for predicting the outcome. By imposing a penalty proportional to the absolute value of the coefficients, LASSO effectively eliminates irrelevant features by shrinking their coefficients to zero.

3. Results and discussion

3.1. Material characterization

Raman spectroscopy is one of the most powerful techniques for GBM characterization since it reveals the graphene-based lattice's vibrational modes. In this framework, several Raman bands can be considered relevant for GBM: The G band, located around 1580 cm^{-1}, is related to in-plane vibrations of the sp^2 hybridized carbon atoms. The D band, located around 1350 cm-1, and the D′ band, located around 1620 cm^{-1}, come from vibration near defects or graphene edges. The D″ band, located at around 1550 cm^{-1}, can be related to the presence of a carbon amorphous phase. Finally, the 2D band (often referred to as G′), located around 2700 cm^{-1}, is a second-order band related to layer stacking [49–51]. In addition, it has been recently reported that the D* band, located at between 1050 and 1200 cm^{-1} originates from the vibrations of carbon atoms restricted by the oxygen-containing groups, i.e., it can be related to the oxidation degree of the crystal structure [52]. It is worth mentioning that the Raman spectra displayed in the following are an average of those obtained solely from a mapping performed on a representative area of the device (Fig. S3 in the Supporting Information).

3.1.1. ME device

The material resulting from the scotch tape method of mechanical exfoliation exhibits characteristics of pristine graphene, graphene in its traditional definition, and can be considered a reference material for the rest of GBM presented in this work. The ME device presents the exfoliated graphene flakes, with irregular shapes, and it is contacted by deposited Au pads acting as electrodes.

A relatively large flake was used for the gas sensing test, as seen by optical microscopy (Fig. 2a). Within, the material presents a largely homogeneous surface dotted with small flakes, typically measuring a few thousand nanometers in lateral size and around 1.6 nm in height (Fig. 2b). The RMS surface roughness is approximately 2.74 nm.

In addition, the bands G and 2D are identified in the Raman spectra (Fig. 2c), giving an I(D)/I(G) ratio of 0 and I(2D)/I(G) ratio of 1.13, agreeing with other examples of near-pristine graphene obtained through this method [49].

3.1.2. CVD850, CVD890 and CVD 935 devices

The CVD-grown series consists of a multi-layered graphene strip with a width of 10 μm and a length of 210 μm placed between two Au electrodes.

In the CVD synthesis method, the process temperature significantly influences the equilibrium between three primary phenomena: adatom capture, surface diffusion, and re-evaporation [53]. Re-evaporation and surface diffusion are impeded at lower process temperatures, promoting the formation of graphene crystalline nuclei. Conversely, higher temperatures facilitate the surface diffusion of adsorbed carbon atoms, leading to the formation of larger, more stable nuclei, and reducing the overall number of nucleation sites, i.e., they hinder the further formation of nuclei in favour of the growth of already existing ones [54]. Additionally, terrace-like structures are observed in the samples grown at higher temperatures, as evidenced in the microscopy and AFM topography images, presented in Fig. 3a–f.

These structures can result from the nucleation and growth of a new graphene layer on top of an existing layer as explained by the "wedding cake" model, which describes the stepwise growth of graphene layers, resulting in a multilayer structure that resembles the tiers of a wedding cake [55]. Large SEM images were analyzed to extract the surface density of these terrace-like structures (Figs. S4–5 in the Supporting Information), which is presented along the AFM-obtained surface roughness in Table S2 in the Supporting Information. For the CVD850 sample, a relatively smooth and homogeneous surface is observed. However, the surface becomes more uneven and heterogeneous as the process temperature increases, which could be related to relatively large crystalline terraces.

The average Raman spectra for the CVD-grown samples are displayed in Fig. S6 in the Supporting Information. Unlike the ME device, the presence of defects is evident with the significant prominence of the D band. Additionally, D*, D″, and D' bands can be deconvoluted for a detailed comparative analysis, by Lorentzian fitting, among each sample. In this regard, the I(D)/I(G) ratio is a commonly used parameter to provide a first approach to the magnitude of structural defects within graphene-based structures. For the CVD-grown devices, values of 0.87,

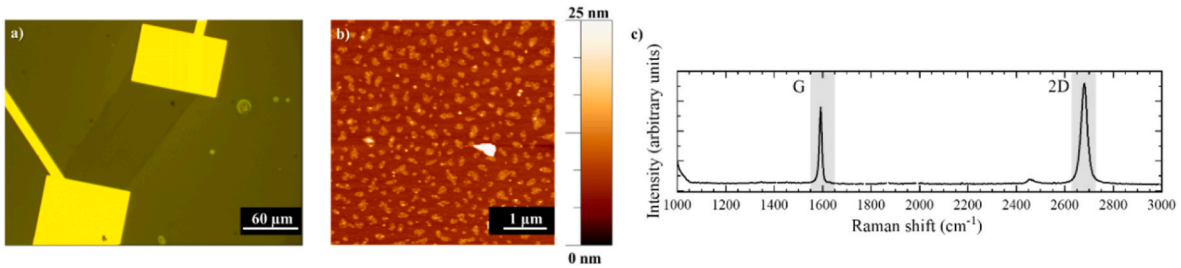

Fig. 2. (a) Optic micrography, (b) AFM image, and (c) broad range average Raman spectrum for the ME device.

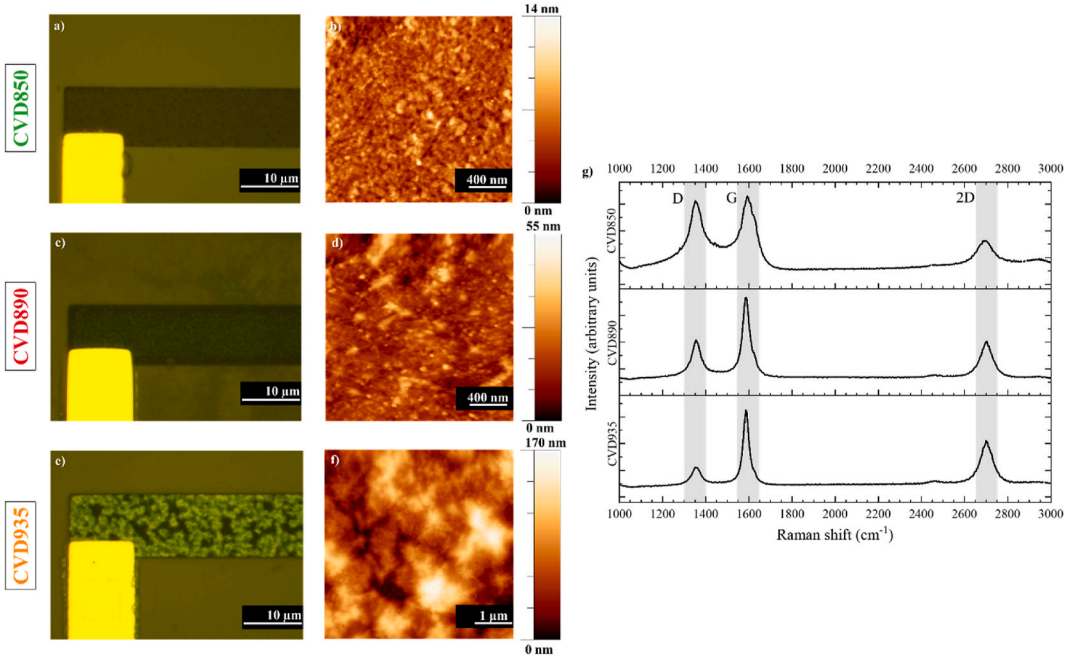

Fig. 3. Optical micrographs and AFM images for CVD850 (a, b, and c, respectively), CVD 890 (d, e, and f, respectively), and CVD935 (g, h, and i, respectively). Broad range average Raman spectrum (j) for the three CVD-based devices, highlighting the main Raman bands for analysis.

0.44, and 0.24 are obtained for the CVD850, CVD890, and CVD935 samples, respectively. This decreasing trend with increasing growth temperature agrees with previous reports [52].

Interestingly, another crucial parameter for characterizing a sensitive GBM is the degree of oxidation, nature of ligands, or chemical functionalization of graphene-based compounds [56,57]. At this point, the I(D*)/I(G) ratio can provide important insights as it relates to the oxygen content in the carbon-based structure [52]. Specifically, the D* band is only relevant for CVD850, resulting in an I(D*)/I(G) ratio of 0.19, whereas, for CVD890 and CVD935, this value is 0.02 and 0.01, respectively. It should be noted that the samples are grown under vacuum conditions, and chemical functionalization through oxidation may occur when highly reactive sites are first exposed to a normal atmosphere.

Furthermore, the activation of the D″ band indicates a certain level of amorphous structure, thus the I(D″)/I(G) ratio can be used to infer the degree of disorder or amorphous character in the samples [52]. For the CVD850 sample, the I(D″)/I(G) ratio is 0.24, which is significantly higher than the ratios for the CVD890 and CVD935 samples, which are 0.04 and 0.05, respectively. This suggests that the CVD850 sample has a higher amorphous content and lower crystallinity compared to the other two samples. As previously indicated, lower growth temperatures, such as 850 °C, can impede crystal growth, leading to smaller crystallites and a more amorphous structure.

Finally, it is also possible to determine the predominant nature of structural defects through the I(D)/I(D′) ratio. This ratio has a value close to ~3.5 when the predominant defects are grain boundaries, about ~7 when they are due to vacancies, and close to ~13 when they are caused by sp^3 hybridizations [28,58]. From the Lorentzian deconvolution of the bands, an I(D)/I(D') ratio ranging from 3.12 for CVD850 to 4.38 and 4.61 for CVD890 and CVD935, respectively, is obtained. This indicates that grain boundaries are the main origin for the lattice discontinuities for all the CVD-grown samples, with a tendency towards vacancy predominance in the samples grown at higher temperatures.

Therefore, the CVD850 sample exhibits a more pronounced amorphous structure with a higher degree of defects, and a greater presence of bound oxygen, compared to samples synthesized at higher temperatures. The latter, CVD890 and CVD935, differ from each other mainly in their surface structure, i.e., roughness and terrace density.

3.1.3. BM100 device

The product of ball milling is classified as FLMG, comprised of agglomerations of non-oxidized few-layered graphene domains into nanoparticles with a mesoporous structure, as comprehensively described elsewhere [32].

As a result of the dielectrophoresis-assisted drop-casting, FLMG nanoparticles are either deposited at the centre of the electrodes or assembled into chains contacting both electrodes in the IDE substrate. Briefly, during the solvent evaporation process, an alternating electrical field induces nanoparticle growth between electrodes. This continues until sufficient contacts are formed, allowing electrical current flow under the applied voltage. An electrical resistance of ~55 Ohm is obtained after the deposit. Fig. 4a and b shows complete and incomplete chains, with a width of approximately 1000 ± 100 nm, roughly the size of a few FLMG nanoparticles.

Furthermore, a significant amount of material appears to be deposited on top of the gold electrodes due to not being affected by the electric field. However, it is worth noting that this portion of the deposit will not significantly participate in the sensing performance of the device.

While the ME and CVD devices are made with bidimensional GBM, BM100 is composed of GBM nanoparticles. The crucial distinction can be better depicted in the SEM image comparison shown in Fig. S7 in the Supporting Information, contrasting BM100 with CVD samples as an example. Consequently, analyzing surface roughness cannot be approached in the same manner as with the previous devices. However, AFM provides a detailed morphology of the nanoparticles, which closely aligns with observations made under SEM. These nanoparticles exhibit irregular shapes; importantly, both the lateral size and height of these nanoparticles are fairly similar, suggesting they could be considered spherical with typical diameters of a few hundred nanometers, consistent with prior observations [18].

Average Raman spectrum is shown in Fig. 4c and reveals a relatively defective material in terms of the I(D)/I(G) ratio with a value of 0.75. However, as opposed to CVD850, the deconvolution analysis presented in Fig. S8 in the Supporting Information reveals an I(D*)/I(G) ratio that suggests a relatively low degree of oxygenated functional groups, with a

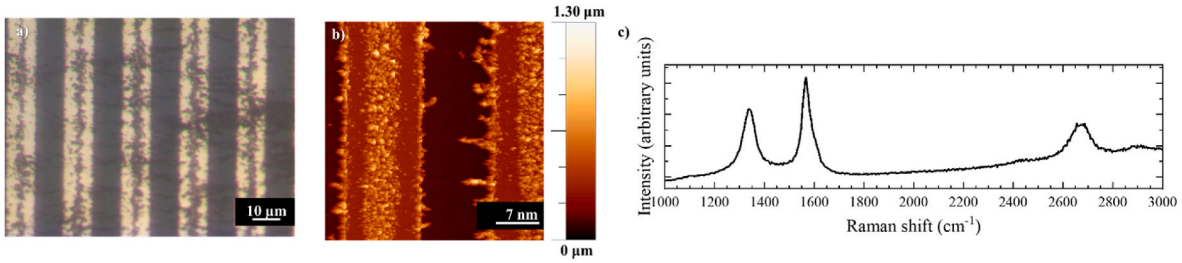

Fig. 4. (a) Optic micrograph, (b) AFM image, and (c) broad range average Raman spectrum for the BM100 device.

value of 0.05. In addition, the deconvolution analysis reveals I(D″)/I(G) and I(D′)/I(G) ratios of 0.13, and 0.22, respectively. In addition to an I(D)/I(D′) ratio of 3.35, similar to that of CVD850 and related to the contribution of grain boundaries to the defect's nature.

3.2. Gas sensing

As discussed, the materials within the studied devices present several differences in their physicochemical characteristic despite being largely classified as non-oxidized GBM. For instance, the rise of additional Raman bands, related to different defects, and the surface modification through terrace structures suggests crucial differences in terms of potential analyte adsorption sites during the gas sensing operation.

The sensing performance of the different devices under all three tests is presented in Fig. 5. Noteworthy, all graphene-based devices exhibited a robust response, in the form of a change in electrical resistance, towards the presence of 1 ppm of NO_2 in air after 15 min of exposure at room temperature, demonstrating their capability to monitor this analyte for different applications. However, there are notable differences worth discussing.

Whereas pristine graphene exhibits neutral conductivity, with a balanced concentration of positive and negative charge carriers [30], most GBM, when used as active material in gas sensors, behave as p-type semiconductors. Under normal atmospheric conditions, contaminants such as oxygen or water are adsorbed onto the materials surface, these molecules undergo a charge transfer process in which they capture electrons from the graphene lattice. Which in turn biases the conductivity of the GBM to p-type [59–61]. This p-type behavior is observed during the NO_2 measurements, i.e., the oxidizer NO_2 draws electrons upon adsorption, decreasing the material's electrical resistance, for all devices except the ME device. In contrast, the ME device increases its resistance during NO_2 exposure, indicating an n-type behavior.

Similar behavior has been observed in the scientific literature, with hypotheses such as n-doping from the substrate [62,63] or photo-induced desorption of the p-type doping adsorbates [64,65] have been proposed to explain it. Further explanations are beyond the scope of the current research, noting that the use and performance of these sensors are not conditioned by the sign of their response but rather by other parameters that are later discussed.

The ME device responds to NO_2 with a mean (3) maximum response of 6.30 ± 3.81 %, with the large deviation being conditioned by the first exposure, a behavior usually observed in gas sensors (see Fig. 5A1). The device exhibits partial recovery and the response is decreased after each exposure. This indicates that even under UV irradiation, the device has limited NO_2 desorption during the 15 min timeframe. Thus, despite ME having the lowest RMS noise value (9 ppm), partial recovery prevents a correct calculation of the LoD value since the sensitivity slope does not converge (Fig. 5B1).

For the p-type behaving devices, their NO_2 sensing performance can be divided into two groups:

In the first group, CVD890 and CVD935 devices display a relatively low amplitude response towards NO_2. Despite being similar in their physicochemical properties, they notably differ in their mean (3) maximum responses are −0.11 ± 0.02 % and −0.84 ± 0.09 % for CVD890 and CVD935, respectively (Fig. 5A3-4). In this case, with a low deviation between runs due to the full recovery that these devices exhibit under UV irradiation. The RMS calculations provide noise values of 82 ppm for CVD890 and 77 ppm for CVD935, which, along with their

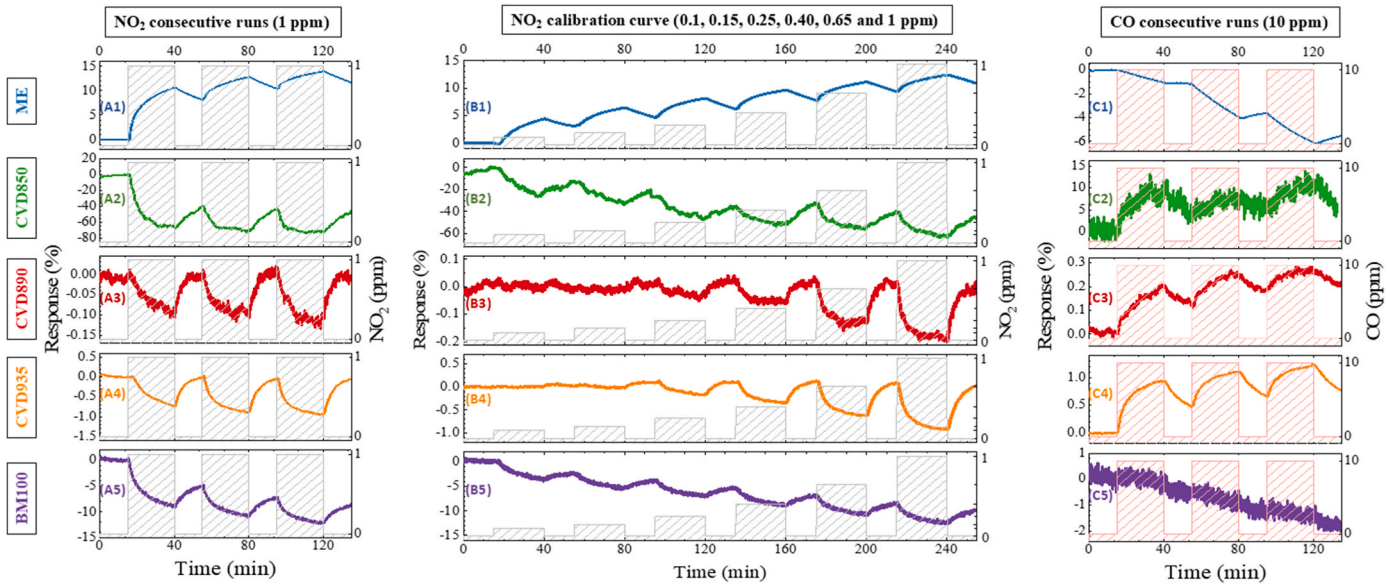

Fig. 5. Real-time responsiveness of ME, CVD850, CVD890, CVD935, and BM100. Figures are presented in lettered columns (A–C) for each sensing test and numbered rows (1–5) for each device.

sensitivity lead to an exceptionally low LoD of 21.74 ± 0.72 and 110.06 ± 2.15 parts per billion (ppb), respectively (Fig. 5B3–4). Notably, these devices exhibit excellent reproducibility, with their response being similar to that of a previous batch fabricated under the same conditions as previously reported [39].

In the second group, CVD850 and BM100 present relatively high amplitude responses with partial recovery that substantially hinders reproducibility and causes a decreased performance across runs. For CVD850, the mean (3) maximum response is −36.00 ± 26.89 %, again with a dispersion heavily affected by the strong partial recovery (Fig. 5A2). The response of CVD850 device during exposure tends to reach saturation, or steady state, causing the largest variation in device resistivity to occur during the first minutes of exposure. This device presents the highest RMS noise with a value of 1.21 % (12.100 ppm). Likewise, for BM100 device, the mean (3) maximum response is −6.63 ± 2.05 % (Fig. 5A5). The response dynamics resemble those of the CVD890 and CVD935 devices despite the differences in the sensing material. Similar to the case of ME device, the LoD of neither CVD850 nor BM100 can be accurately calculated with Equation (2) due to the strong partial recovery effect (Fig. 5B2 and B5).

Interestingly, a similar analysis can be applied to the CO tests presented in Fig. 5C1-5. The ME device further confirms its n-type behavior, i.e., a decrease in the resistance upon an electron-donating effect of CO (Fig. 5C1) [15,60], similarly, the rest of the devices further confirm their p-type behavior.

CVD890 and CVD935 devices respond to 10 ppm of CO with a variation of 0.14 ± 0.06 % and 0.71 ± 0.20 %, respectively, a similar magnitude to their response towards NO_2, with a slight partial recovery. All the results suggest that these devices work analogously towards oxidizing and reducing gaseous analytes, as previously reported [39]. In contrast, CVD850 device exhibits a response to CO with a mean (3) value of 5.98 ± 2.56 %, barely distinguishable from the device's noise, whereas BM100 exhibits no response whatsoever (Fig. 5C2 and C5). Interestingly, CVD850 and BM100 devices show the larger response towards 1 ppm of NO_2 and the lowest towards 10 ppm of CO, exhibiting excellent selectivity.

Thus, significant differences are observed among the five different non-oxidized graphene-based chemiresistive gas sensors. While all of them can be used as sub-ppm NO_2 gas sensors, their differences in terms of response magnitude, recovery capability, noise ratio, and specificity toward other analytes can substantially influence their potential applications. These differences can be better understood through careful correlation analysis and interpretation of the comprehensive characterization previously presented.

3.3. Correlation analysis

To further elucidate the sensing behavior of this collection of non-oxidized graphene-based sensors, a systematic correlation analysis between the material's properties and the sensor's performance metrics was performed through LASSO regression technique. The dataset from structural characterization includes a large number of features, the terrace density and the different Raman ratios (I(D), I(D*), I(2D) and I(D″) over I(G)) and the base resistance (Ohm) and its noise (ppm), some of which may be irrelevant or have minimal impact on specific target variables, the mean maximum responses to NO_2 and CO, as well as a selectivity parameter obtained through the coefficient of the previous. For direct inspection, the values of the ratios between the amplitudes of the main Raman modes were used are shown in Table 1.

Fig. 6 and Table S3 in the Supporting Information show the primary and secondary discriminant parameters for each pair of samples, obtained by the LASSO regression technique. The results illustrated in Fig. 6 can be interpreted as the following example: The most accurate parameter to distinguish between the ME and the CVD935 device, in terms of their response to NO_2 and CO is the I(2D)/I(G) - which had a value of 1.13 for ME and 0.56 for CVD935 -. This is also true to distinguish between ME and CVD890, as expected from the similarity between CVD890 and CVD935.

Table 1
Values of the amplitude ratios of the main Raman modes obtained by Lorentzian fitting.

Raman ratios	ME	CVD850	CVD890	CVD935	BM100
I(2D)/I(G)	1.13	0.41	0.45	0.56	0.46
I(D)/I(G)	~0	0.87	0.44	0.29	0.75
I(D*)/I(G)	~0	0.19	0.02	0.01	0.05
I(D″)/I(G)	~0	0.24	0.04	0.03	0.13
I(D′)/I(G)	~0	0.28	0.10	0.05	0.22

Henceforth, the LASSO method shows some notable results. For instance, the I(D*)/I(G) parameter discriminates between the relatively defective devices and the rest, when analyzing their responses to both NO_2 and CO, more accurately than the I(D)/I(G). Meaning that, for such devices, it is not the overall defectivity of the device which mainly conditions their sensing performance, but rather the ratio related to the oxygen-containing groups. The I(D*)/I(G) parameter is also relevant to distinguish between the two relatively defective materials – CVD850 and BM100 -.

Notably, for some sets of devices, CVD935 vs BM100 and CVD890 vs BM100, the parameters to distinguish the sensors in terms of their response towards NO_2 and CO differ. Essentially revealing that the sensing mechanisms for both analytes are mainly affected by different physicochemical parameters. Results suggest that, for CO detection, the terraces play the main role, whereas for NO_2, the mechanisms at play would be more related to the amorphization or presence of oxygen-containing groups.

Overall, the I(D)/I(G) ratio appears to be relevant to the device's discrimination only when highly pristine (ME) and relatively highly defective (CVD850 and BM100) materials are compared.

3.4. Summary

Defects within the graphene structure significantly influence the performance of graphene-based sensors. Although the I(D)/I(G) Raman ratio is commonly used to correlate these defects, it has limited accuracy in capturing the specific nature of these defects. Additionally, members of the graphene-based material family may behave like different material systems, affecting the relationship between their physicochemical properties and sensing performance. It has been proven here that more often, the nature of defects, represented by I(D″)/I(G), related to the carbon amorphous phase, or I(D*)/I(G), related to oxygen-containing groups, are best suited to understand the graphene-based gas sensors sensitivity and selectivity.

Here it is shown that through a controlled application of the CVD technique, where temperature is a critical factor, the structural ordering of the resulting GBM can be manipulated, as observed in the Raman spectra through the D″ band.

To enhance sensitivity while also maintaining selectivity in a device, keeping a high level of amorphization with a low degree of oxidation proves effective. Specifically, a CVD-synthesized GBM grown at a temperature of 850 °C exhibited a high degree of amorphization. This structural characteristic conferred the device with exceptionally high sensitivity to NO_2 with good selectivity against CO. This approach was further demonstrated with the ball-milled BM100 device. Additionally, the selectivity was correlated with the D″ and D bands observed in the Raman spectra, illustrating the relationship between these structural characteristics and the sensor's performance.

As the temperature in the CVD process is increased, there is a corresponding decrease in amorphization, as evidenced when comparing samples CVD890 and CVD935 with CVD850. The higher crystallinity leads to an increase in the response towards CO, achieving detection capabilities below the recommended exposure limits. This suggests a

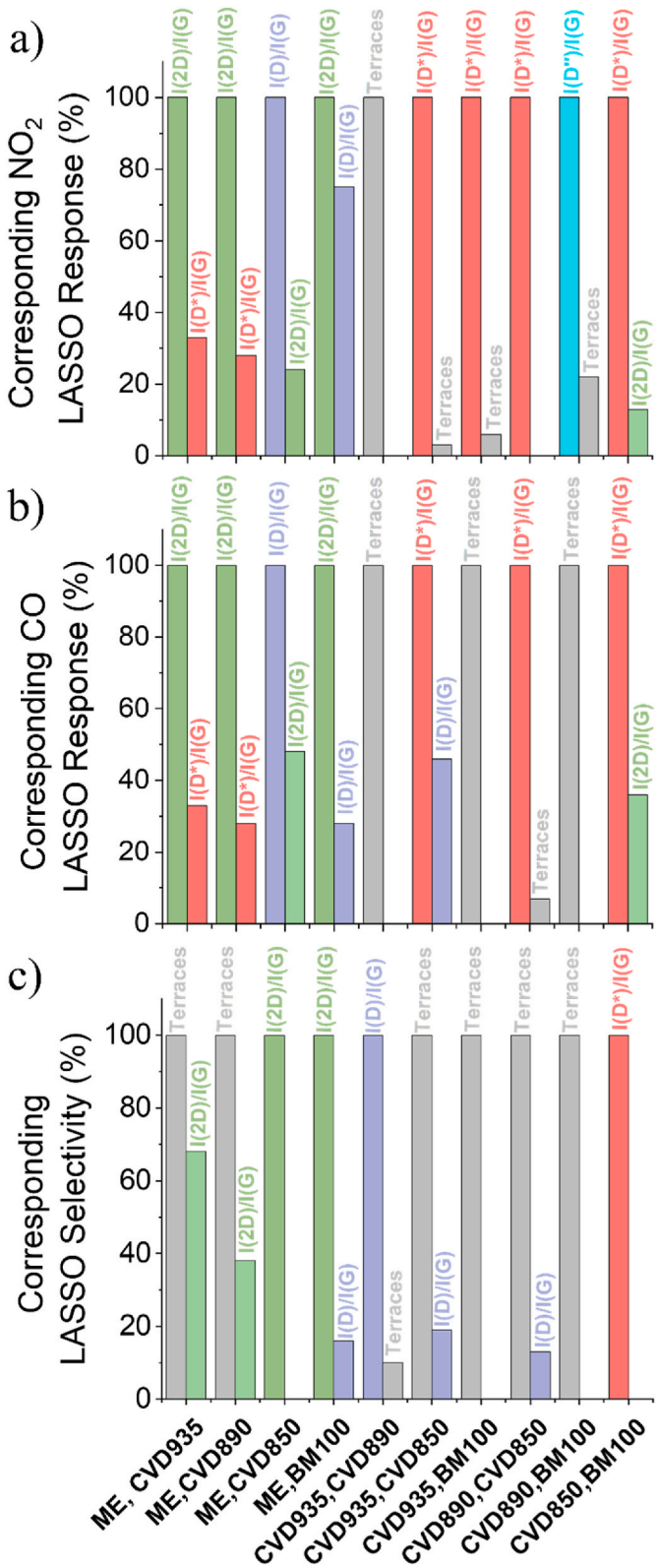

Fig. 6. The primary and secondary discriminant parameters for each sample pair, obtained from the LASSO technique, a) Corresponding NO_2 LASSO Response (%), Corresponding CO LASSO Response (%), and c) Corresponding LASSO Selectivity (%).

positive dependence between amorphization and selectivity, as also observed in the mechanically exfoliated GBM device ME.

Finally, the formation of terrace structures at higher CVD temperatures suggests the generation of reactive sites that improve sensitivity towards both tested analytes with exceptional desorption and recovery characteristics.

4. Conclusions

This work showcases five different sensors based on non-oxidized graphene-based materials (GBM). All sensors are capable of detecting NO_2 at room temperature, even at sub-ppm concentration levels below the human toxicity threshold. However, they exhibit markedly different sensing performances.

In this study, we investigated NO_2 detection using sensors based on GBM, ranging from highly amorphous carbon to quasi-pristine graphene. The number and nature of defects in these materials are critical in correlating their structure with the sensor's response to NO_2 and CO, and in determining their selectivity. We explored various types of defects, including amorphization, oxidation, and nucleation terraces, which resulted in a diverse range of responses. Quasi-pristine graphene exhibited a strong response but lacked selectivity. In contrast, Few-Layered Mesoporous Graphene (FLMG) displayed high sensitivity to NO_2 and complete immunity to CO. Additionally, nucleation terraces induced by higher temperatures in CVD-grown graphene-based sensors enhanced sensitivity but did not improve selectivity in the response.

For similar GBM, especially those obtained from the same method with slight variations, it is crucial to consider a variety of characteristic parameters. This work demonstrates that advanced analysis of Raman spectroscopy is sufficient to derive most parameters that effectively differentiate between non-oxidized GBM exhibiting distinct sensing behaviors. By employing LASSO regression, we ensured empirical results free from subjective correlations, identifying key parameters governing gas response behavior. This approach paves the way for designing graphene-based sensor arrays that capitalize on graphene's room temperature operation and its varied sensing performances for advanced applications.

The ultimate aim is to develop efficient processes for producing GBM with customized gas sensing characteristics, hence offering a framework for additional investigation into the thorough morphological and structural characterisation of defects in carbon-based gas sensor samples. Based on this research, there is a significant opportunity to create databases for the efficient pre-design of defect-containing materials. This approach could extend to utilizing deep learning techniques for accurately predicting sensor responses, thereby advancing novel methods in gas sensor fabrication.

CRediT authorship contribution statement

Álvaro Peña: Writing – review & editing, Writing – original draft, Validation, Methodology, Investigation, Data curation, Conceptualization. **Jesús López-Sánchez:** Writing – review & editing, Writing – original draft, Validation, Methodology, Investigation, Data curation. **Leandro Sacco:** Writing – review & editing, Methodology, Investigation, Conceptualization. **Sten Vollebregt:** Writing – review & editing, Investigation. **Jorge Marqués-Marchán:** Writing – review & editing, Methodology, Investigation. **M. Carmen Horrillo:** Writing – review & editing, Supervision, Project administration, Funding acquisition. **Pilar Marín:** Writing – review & editing, Supervision, Project administration, Funding acquisition. **Daniel Matatagui:** Writing – review & editing, Writing – original draft, Supervision, Methodology, Investigation, Data curation, Conceptualization.

Associated content

A supporting document including (S1) Optical micrographs of the

CVD-based devices, (S2) I–V curve recorded on the resistor based on BM100 device, (S3) In-plane Raman analyses of the sensor devices, (S4) Representative examples of the binarization process, (S5) SEM raw data employed for the binarization process, is available, (S6) Raman analyses for CVD-samples, (S7) SEM images for BM100 and CVD-samples prepared at 850, 890, and 935 °C, S(8) Raman analyses for BM100 sample, (Table S1) Collection of previously reported graphene-based gas sensors studies based on defect engineering approach, (Table S2) RMS roughness and terrace density percentage values obtained from representative areas of the CVD850, CVD890, and CVD935 devices, and (Table S3) LASSO technique results.

Funding information

Author A. P. received funding from grant PRE2019-0875001234, Ministerio de Ciencia e Innovación (MCIN), Spain. Authors A. P., D. M., P. M., and M-C. H. received funding from project PDC2022-133039-I00 and PID2021-123112OB-C21 from MCIN/AEI/10.13039/501100011033, Spain and European Union Next Generation EU/PRTR. D. M. acknowledges financial support from grant RYC2021-031166-I funded by MCIU/AEI/10.13039/501100011033. J. L.-S. acknowledges the financial support from PID2023-151036OA-I00 funded by MCIU/AEI/10.13039/501100011033 and by the European Union, and from grant RYC2022-035912-I funded by MCIU/AEI/10.13039/501100011033 and by the European Social Fund Plus (ESF+). JM thanks the Regional Government of Madrid for the project P2018/NMT-4321 NANOMAGCOST. M-C. H acknowledges the support from the COST Action CA21101.

Declaration of competing interest

The authors declare that they have no known competing financial interests or personal relationships that could have appeared to influence the work reported in this paper.

Acknowledgements

A. P. and J. M acknowledge and thank the contribution of Agustina Asenjo from ICMM in the AFM-related characterization. A. P. acknowledges the support provided by Paula Moreno from ITEFI during the gas sensing tests. A. P. acknowledges the support of Filiberto Ricciardella from TU Delft and Mario Miscuglio from the University of Genova in fabricating the devices.

Raman spectroscopy characterization was performed at Instituto de Cerámica y Vidrio (ICV–CSIC, Spain). Standard optical microscope was used at Instituto de Magnetismo Aplicado (IMA - UCM, Spain). AFM characterization was performed at Instituto de Ciencia de Materiales (ICMM – CSIC, Spain). Electron microscopy was performed at Centro Nacional de Microscopía Electrónica (CNME, Spain). Sensor testing took place at Instituto de Tecnologías Físicas y de la Información (ITEFI, Spain).

Appendix A. Supplementary data

Supplementary data to this article can be found online at https://doi.org/10.1016/j.talanta.2024.127507.

Data availability

Data will be made available on request.

References

[1] R. Schmalensee, P.L. Joskow, A.D. Ellerman, J.P. Montero, E.M. Bailey, An interim evaluation of sulfur dioxide emissions trading, J. Econ. Perspect. 12 (1998) 53–68, https://doi.org/10.1257/jep.12.3.53.

[2] World Health Organization (WHO), Air Quality Guidelines for Europe, second ed., WHO regional publications, 2000.

[3] U. Latza, S. Gerdes, X. Baur, Effects of nitrogen dioxide on human health: systematic review of experimental and epidemiological studies conducted between 2002 and 2006, Int. J. Hyg Environ. Health 212 (2009) 271–287, https://doi.org/10.1016/j.ijheh.2008.06.003.

[4] American Conference of Governmental Industrial Hygienists (ACGIH), TLVs ® and BEIs ® Based on the Documentation of the ® Defining the Science of Occupational and Environmental Health ® Threshold Limit Values for Chemical Substances and Physical Agents Biological Exposure Indices, 2019. Cincinnati, OH, USA.

[5] T.W. Hesterberg, W.B. Bunn, R.O. McClellan, A.K. Hamade, C.M. Long, P. A. Valberg, Critical review of the human data on short-term nitrogen dioxide (NO_2) exposures: Evidence for NO_2 no-effect levels, Crit. Rev. Toxicol. 39 (2009) 743–781, https://doi.org/10.3109/10408440903294945.

[6] Betzaida Tejada-Vera, QuickStats: number of deaths resulting from unintentional carbon monoxide poisoning,* by month and year — national vital statistics system, United States, 2010–2015, MMWR Morb. Mortal. Wkly. Rep. 66 (2017) 234, https://doi.org/10.15585/mmwr.mm6608a9.

[7] World Health Organization, WHO Global Air Quality Guidelines: Particulate Matter (PM2.5 and PM10), Ozone, Nitrogen Dioxide, Sulfur Dioxide and Carbon Monoxide, 2021.

[8] M.A.H. Khan, M.V. Rao, Q. Li, Recent advances in electrochemical sensors for detecting toxic gases: NO_2, SO_2 and H_2S, Sensors 19 (2019) 905, https://doi.org/10.3390/s19040905.

[9] L. Kaur, Graphene based chemiresistor sensors for the detection of toxic air pollutants: a theoretical overview, J. Indian Chem. Soc. 100 (2023) 101019, https://doi.org/10.1016/j.jics.2023.101019.

[10] R. Ghosh, M. Aslam, H. Kalita, Graphene derivatives for chemiresistive gas sensors: a review, Mater. Today Commun. 30 (2022) 103182, https://doi.org/10.1016/j.mtcomm.2022.103182.

[11] F. Schedin, A.K. Geim, S. V Morozov, E.W. Hill, P. Blake, M.I. Katsnelson, K. S. Novoselov, Detection of individual gas molecules adsorbed on graphene, Nature 6 (2007) 652–655, https://doi.org/10.1038/nmat1967.

[12] J. Wang, B. Singh, J.-H. Park, S. Rathi, I. Lee, S. Maeng, H.-I. Joh, C.-H. Lee, G.-H. Kim, Dielectrophoresis of graphene oxide nanostructures for hydrogen gas sensor at room temperature, Sensor. Actuator. B Chem. 194 (2014) 296–302, https://doi.org/10.1016/j.snb.2013.12.009.

[13] S. Huang, L.A. Panes-Ruiz, A. Croy, M. Löffler, V. Khavrus, V. Bezugly, G. Cuniberti, Highly sensitive room temperature ammonia gas sensor using pristine graphene: the role of biocompatible stabilizer, Carbon NY 173 (2021) 262–270, https://doi.org/10.1016/j.carbon.2020.11.001.

[14] F. Ricciardella, S. Vollebregt, T. Polichetti, B. Alfano, E. Massera, P.M. Sarro, An Innovative Approach to Overcome Saturation and Recovery Issues of CVD Graphene-Based Gas Sensors, IEEE SENSORS, Glasgow, UK, 2017, pp. 1–3, https://doi.org/10.1109/ICSENS.2017.8234284, 2017.

[15] X. Yan, Y. Wu, R. Li, C. Shi, R. Moro, Y. Ma, L. Ma, High-performance UV-assisted NO_2 sensor based on chemical vapor deposition graphene at room temperature, ACS Omega 4 (2019) 14179–14187, https://doi.org/10.1021/acsomega.9b00935.

[16] Z. Zhang, Z. Gao, R. Fang, H. Li, W. He, C. Du, UV-assisted room temperature NO_2 sensor using monolayer graphene decorated with SnO_2 nanoparticles, Ceram. Int. 46 (2020) 2255–2260, https://doi.org/10.1016/j.ceramint.2019.09.211.

[17] S. Ann Jose, Y. Atwa, J. Mao, H. Shakeel, Restoring adsorption properties of graphene sensor with printable glass encapsulation using UV illumination, FlatChem 40 (2023) 100510, https://doi.org/10.1016/j.flatc.2023.100510.

[18] D. Matatagui, J. López-Sánchez, A. Peña, A. Serrano, A. del Campo, O.R. de la Fuente, N. Carmona, E. Navarro, P. Marín, M. del Carmen Horrillo, Ultrasensitive NO_2 gas sensor with insignificant NH_3-interference based on a few-layered mesoporous graphene, Sensor. Actuator. B Chem. 335 (2021) 129657, https://doi.org/10.1016/j.snb.2021.129657.

[19] S. Deb, A. Mondal, Y. Ashok Kumar Reddy, Review on development of metal-oxide and 2-D material based gas sensors under light-activation, Curr. Opin. Solid State Mater. Sci. 30 (2024) 101160, https://doi.org/10.1016/j.cossms.2024.101160.

[20] W. Yuan, G. Shi, Graphene-based gas sensors, J. Mater. Chem. A Mater 1 (2013) 10078–10091, https://doi.org/10.1039/c3ta11774j.

[21] Y. You, J. Deng, X. Tan, N. Gorjizadeh, M. Yoshimura, S.C. Smith, V. Sahajwalla, R. K. Joshi, On the mechanism of gas adsorption for pristine, defective and functionalized graphene, Phys. Chem. Chem. Phys. 19 (2017) 6051–6056, https://doi.org/10.1039/c6cp07654h.

[22] S. Bandi, A.K. Srivastav, Chapter Seven: graphene-based chemiresistive gas sensors, Compr. Anal. Chem. 91 (2020) 149–173, https://doi.org/10.1016/bs.coac.2020.08.006.

[23] L. Guo, T. Li, Sub-ppb and ultra selective nitrogen dioxide sensor based on sulfur doped graphene, Sensor. Actuator. B Chem. 255 (2018) 2258–2263, https://doi.org/10.1016/j.snb.2017.09.021.

[24] Z. Chen, J. Wang, Y. Wang, Strategies for the performance enhancement of graphene-based gas sensors: a review, Talanta 235 (2021) 122745, https://doi.org/10.1016/j.talanta.2021.122745.

[25] F. Ricciardella, S. Vollebregt, T. Polichetti, M. Miscuglio, B. Alfano, M.L. Miglietta, E. Massera, G. Di Francia, P.M. Sarro, Effects of graphene defects on gas sensing properties towards NO_2 detection, Nanoscale 9 (2017) 6085–6093, https://doi.org/10.1039/c7nr01120b.

[26] S. Yeo, C.Y. Lee, D.-S. Kim, Y.S. Hwang, J.K. Park, M.-H. Jung, W.-J. Cho, J.S. Lee, C. Kim, Sensing response enhancement of graphene gas sensors by ion beam bombardment, Thin Solid Films 677 (2019) 73–76, https://doi.org/10.1016/j.tsf.2019.03.026.

[27] Y.-H. Zhang, Y.-B. Chen, K.-G. Zhou, C.-H. Liu, J. Zeng, H.-L. Zhang, Y. Peng, Improving gas sensing properties of graphene by introducing dopants and defects: a first-principles study, Nanotechnology 20 (2009) 185504, https://doi.org/10.1088/0957-4484/20/18/185504.
[28] A. Eckmann, A. Felten, A. Mishchenko, L. Britnell, R. Krupke, K.S. Novoselov, C. Casiraghi, Probing the nature of defects in graphene by Raman spectroscopy, Nano Lett. 12 (2012) 3925–3930, https://doi.org/10.1021/nl300901a.
[29] ISO/TS 80004-13, Graphene and Related Two-Dimensional (2D) Materials, International Organization for Standardization, Geneva, 2017.
[30] K.S. Novoselov, A.K. Geim, S.V. Morozov, D. Jiang, Y. Zhang, S.V. Dubonos, I. V. Grigorieva, A.A. Firsov, Electric field effect in atomically thin carbon films, Science 306 (2004) 666–669, https://doi.org/10.1126/science.1102896.
[31] F. Ricciardella, S. Vollebregt, T. Polichetti, B. Alfano, E. Massera, P.M. Sarro, Low temperature CVD grown graphene for highly selective gas sensors working under ambient conditions, Proceedings 1 (2017) 445, https://doi.org/10.3390/proceedings1040445.
[32] J. López-Sánchez, Á. Peña, A. Serrano, A. Del Campo, O. Rodríguez de la Fuente, N. Carmona, D. Matatagui, M.C. Horrillo, J. Rubio-Zuazo, E. Navarro, P. Marín, Generation of defective few-layered graphene mesostructures by high-energy ball milling and their combination with FeSiCuNbB microwires for reinforcing microwave absorbing properties, ACS Appl. Mater. Interfaces 15 (2023) 3507–3521, https://doi.org/10.1021/acsami.2c19886.
[33] F. Ricciardella, S. Vollebregt, T. Polichetti, B. Alfano, E. Massera, P.M. Sarro, High Sensitive Gas Sensors Realized by a Transfer-free Process of CVD Graphene, IEEE SENSORS, Orlando, FL, USA, 2016, pp. 1–3, https://doi.org/10.1109/ICSENS.2016.7808638, 2016.
[34] F. Ricciardella, T. Polichetti, S. Vollebregt, B. Alfano, E. Massera, P.M. Sarro, Analysis of a calibration method for non-stationary CVD multi-layered graphene-based gas sensors, Nanotechnology 30 (2019) 385501, https://doi.org/10.1088/1361-6528/ab2aac.
[35] Patent Spanish, P. Marín, E. Navarro, J. López-Sánchez, A. Peña, M.C. Horrillo, D. Matatagui, Obtención a gran escala en un solo paso y a temperatura ambiente de material compuesto por pocas láminas de grafeno con un alto grado de defectos mediante molienda mecánica seca oscilatoria de alta energía, 2021. ES2779151B2.
[36] J. López-Sánchez, A. Serrano, A. del Campo, Á. Muñoz-Noval, E. Salas-Colera, M. Cabero, M. Varela, M. Abuín, G.R. Castro, J. Rubio-Zuazo, Ó. Rodríguez de la Fuente, N. Carmona, A combined micro-Raman, X-ray absorption and magnetic study to follow the glycerol-assisted growth of epsilon-iron oxide sol-gel coatings, J. Alloys Compd. 892 (2022) 162061, https://doi.org/10.1016/j.jallcom.2021.162061.
[37] I. Horcas, R. Fernández, J.M. Gómez-Rodríguez, J. Colchero, J. Gómez-Herrero, A. M. Baro, WSXM: a software for scanning probe microscopy and a tool for nanotechnology, Rev. Sci. Instrum. 78 (2007) 013705, https://doi.org/10.1063/1.2432410.
[38] S. Vollebregt, B. Alfano, F. Ricciardella, A.J.M. Giesbers, Y. Grachova, H.W. van Zeijl, T. Polichetti, P.M. Sarro, A transfer-free wafer-scale CVD graphene fabrication process for MEMS/NEMS sensors. 2016 IEEE 29th International Conference on Micro Electro Mechanical Systems (MEMS), Shangai, China, 2016, pp. 17–20, https://doi.org/10.1109/MEMSYS.2016.7421546.
[39] A. Peña, D. Matatagui, F. Ricciardella, L. Sacco, S. Vollebregt, D. Otero, P. Marín, M.C. Horrillo, Optimization of multilayer graphene-based gas sensors by ultraviolet photoactivation, Appl. Surf. Sci. 610 (2023) 155393, https://doi.org/10.1016/j.apsusc.2022.155393.
[40] K. Drozdowska, A. Rehman, J. Smulko, S. Rumyantsev, B. Stonio, A. Krajewska, M. Słowikowski, M. Filipiak, P. Sai, G. Cywiński, Enhanced gas sensing by graphene-silicon Schottky diodes under UV irradiation, Sensor. Actuator. B Chem. 396 (2023) 134586, https://doi.org/10.1016/j.snb.2023.134586.
[41] F. Ricciardella, S. Vollebregt, R. Tilmann, O. Hartwig, C. Bartlam, P.M. Sarro, H. Sachdev, G.S. Duesberg, Influence of defect density on the gas sensing properties of multi-layered graphene grown by chemical vapor deposition, Carbon Trends 3 (2021) 100024, https://doi.org/10.1016/j.cartre.2021.100024.
[42] A. D'Amico, C. Di Natale, A contribution on some basic definitions of sensors properties, IEEE Sensor. J. 1 (2001) 183–190, https://doi.org/10.1109/JSEN.2001.954831.
[43] A. Peña, J.D. Aguilera, D. Matatagui, P. de la Presa, C. Horrillo, A. Hernando, P. Marín, Real-time monitoring of breath biomarkers with a magnetoelastic contactless gas sensor: a proof of concept, Biosensors 12 (2022) 871, https://doi.org/10.3390/bios12100871.
[44] J.D. Aguilera, D. Arranz, A. Peña, P. Marín, M.C. Horrillo, P. de la Presa, D. Matatagui, Real-time monitoring of breath biomarkers using magnonic wireless sensor based on magnetic nanoparticles, Sens. Biosensing Res. 43 (2024) 100629, https://doi.org/10.1016/j.sbsr.2024.100629.
[45] G.L. Long, J.D. Winefordner, Limit of detection a closer look at the IUPAC definition, Anal. Chem. 55 (1983) 712A–724A, https://doi.org/10.1021/ac00258a724.
[46] Limit of detection in analysis, in: The IUPAC Compendium of Chemical Terminology, International Union of Pure and Applied Chemistry (IUPAC), Research Triangle Park, 2014, https://doi.org/10.1351/goldbook.L03540. NC.
[47] R. Tibshirani, Regression shrinkage and selection via the Lasso, J. R. Stat. Soc. Series B Stat. Methodol. 58 (1996) 267–288, https://doi.org/10.1111/j.2517-6161.1996.tb02080.x.
[48] P. Bickel, P. Diggle, S. Fienberg, U. Gather, I. Olkin, S. Zeger, The Elements of Statistical Learning Data Mining, Inference, and Prediction, Second, Springer, 2009, https://doi.org/10.1007/978-0-387-84858-7.
[49] L.M. Malard, M.A. Pimenta, G. Dresselhaus, M.S. Dresselhaus, Raman spectroscopy in graphene, Phys. Rep. 473 (2009) 51–87, https://doi.org/10.1016/j.physrep.2009.02.003.
[50] S. Vollebregt, R. Ishihara, F.D. Tichelaar, Y. Hou, C.I.M. Beenakker, Influence of the growth temperature on the first and second-order Raman band ratios and widths of carbon nanotubes and fibers, Carbon NY 50 (2012) 3542–3554, https://doi.org/10.1016/j.carbon.2012.03.026.
[51] R. Muzyka, S. Drewniak, T. Pustelny, M. Chrubasik, G. Gryglewicz, Characterization of graphite oxide and reduced graphene oxide obtained from different graphite precursors and oxidized by different methods using Raman spectroscopy, Materials 11 (2018) 15–17, https://doi.org/10.3390/ma11071050.
[52] A.Y. Lee, K. Yang, N.D. Anh, C. Park, S.M. Lee, T.G. Lee, M.S. Jeong, Raman study of D* band in graphene oxide and its correlation with reduction, Appl. Surf. Sci. 536 (2021) 147990, https://doi.org/10.1016/j.apsusc.2020.147990.
[53] V.N.E. Robinson, J.L. Robins, Nucleation kinetics of gold deposited onto UHV cleaved surfaces of NaCl and KBr, Thin Solid Films 20 (1974) 155–175, https://doi.org/10.1016/0040-6090(74)90043-1.
[54] S. Chaitoglou, E. Bertran, Effect of temperature on graphene grown by chemical vapor deposition, J. Mater. Sci. 52 (2017) 8348–8356, https://doi.org/10.1007/s10853-017-1054-1.
[55] R. Xue, I.H. Abidi, Z. Luo, Domain size, layer number and morphology control for graphene grown by chemical vapor deposition, Funct. Mater. Lett. 10 (2017) 1730003, https://doi.org/10.1142/S1793604717300031.
[56] T.A. Saleh, G. Fadillah, Recent trends in the design of chemical sensors based on graphene–metal oxide nanocomposites for the analysis of toxic species and biomolecules, TrAC Trends Anal. Chem. (Reference Ed.) 120 (2019) 115660, https://doi.org/10.1016/j.trac.2019.115660.
[57] R. Valand, A. Sivaiah, Chapter Thirteen: graphene oxide based gas sensors, Compr. Anal. Chem. 106 (2024) 373–390, https://doi.org/10.1016/bs.coac.2024.05.001.
[58] V. León, A.M. Rodriguez, P. Prieto, M. Prato, E. Vázquez, Exfoliation of graphite with trriazine derivatives under ball-milling conditions: preparation of few-layer graphene via selective noncovalent interactions re, ACS Nano 8 (2014) 563–571, https://doi.org/10.1021/nn405148t.
[59] J.D. Fowler, M.J. Allen, V.C. Tung, Y. Yang, R.B. Kaner, B.H. Weiller, Practical chemical sensors from chemically derived graphene, ACS Nano 3 (2009) 301–306, https://doi.org/10.1021/nn800593m.
[60] R.K. Joshi, H. Gomez, F. Alvi, A. Kumar, Graphene films and ribbons for sensing of O_2, and 100 ppm of CO and NO_2 in practical conditions, J. Phys. Chem. C 114 (2010) 6610–6613, https://doi.org/10.1021/jp100343d.
[61] S. Basu, P. Bhattacharyya, Recent developments on graphene and graphene oxide based solid state gas sensors, Sensor. Actuator. B Chem. 173 (2012) 1–21, https://doi.org/10.1016/j.snb.2012.07.092.
[62] L. Ju, J. Velasco, E. Huang, S. Kahn, C. Nosiglia, H.-Z. Tsai, W. Yang, T. Taniguchi, K. Watanabe, Y. Zhang, G. Zhang, M. Crommie, A. Zettl, F. Wang, Photoinduced doping in heterostructures of graphene and boron nitride, Nat. Nanotechnol. 9 (2014) 348–352, https://doi.org/10.1038/nnano.2014.60.
[63] J. Park, R. Rautela, N. Alzate-Carvajal, S. Scarfe, L. Scarfe, L. Alarie, A. Luican-Mayer, J.M. Ménard, UV illumination as a method to improve the performance of gas sensors based on graphene field-effect transistors, ACS Sens. 6 (2021) 4417–4424, https://doi.org/10.1021/acssensors.1c01783.
[64] P. Sun, M. Zhu, K. Wang, M. Zhong, J. Wei, D. Wu, Y. Cheng, H. Zhu, Photoinduced molecular desorption from graphene films, Appl. Phys. Lett. 101 (2012) 053107, https://doi.org/10.1063/1.4742147.
[65] A. Ali, S.-Y. Kim, M. Hussain, S.H.A. Jaffery, G. Dastgeer, S. Hussain, B.T.P. Anh, J. Eom, B.H. Lee, J. Jung, Deep-ultraviolet (DUV)-induced doping in single channel graphene for pn-junction, Nanomaterials 11 (2021) 3003, https://doi.org/10.3390/nano11113003.